

High-Time-Resolution Measurements of the Polarization of the Crab Pulsar at 1.38 GHz

Agnieszka Słowikowska¹, Benjamin W. Stappers², Alice K. Harding³, Stephen L. O'Dell⁴,
Ronald F. Elsner⁴, Alexander J. van der Horst⁵, Martin C. Weisskopf⁴

ABSTRACT

Using the Westerbork Synthesis Radio Telescope (WSRT), we obtained high-time-resolution measurements of the full (linear and circular) polarization of the Crab pulsar. Taken at a resolution of $1/8192$ of the 34-ms pulse period (i.e., $4.1 \mu\text{s}$), the 1.38-GHz linear-polarization measurements are in general agreement with previous lower-time-resolution 1.4-GHz measurements of linear polarization in the main pulse (MP), in the interpulse (IP), and in the low-frequency precursor (LFP). Consistent with previous measurements, we find the MP and LP to be linearly polarized at about 24% and 21%, with no discernible difference in polarization position angle. Furthermore, we find no evidence for variation (sweep) in polarization position angle over the MP, the IP, or the LFP. However, the main pulse exhibits a small but statistically significant quadratic variation in the degree of linear polarization. In addition, we detect weak circular polarization in the main pulse and interpulse, and strong ($\approx 20\%$) circular polarization in the low-frequency precursor, which also exhibits very strong ($\approx 98\%$) linear polarization at a position angle about 40° from that of the MP or IP. The pulse-mean polarization properties are consistent with the LFP being a low-altitude core component and the MP and IP being high-altitude caustic components. However, current models for the MP and IP emission do not readily account for the observed absence of pronounced polarization changes across the pulse.

¹Kepler Institute of Astronomy, University of Zielona Góra, Lubuska 2, 65-265 Zielona Góra, Poland

²Jodrell Bank Centre for Astrophysics, University of Manchester, Manchester M13 9PL, UK

³Astrophysics Science Division, NASA Goddard Space Flight Center, Greenbelt, MD 20771, USA

⁴Astrophysics Office, NASA Marshall Space Flight Center, ZP12, Huntsville, AL 35812, USA

⁵Astronomical Institute, University of Amsterdam, Science Park 904, 1098 XH Amsterdam, The Netherlands

Peripheral to the polarimetry, we find high-frequency substructure in the profile of the main pulse, presumably due to giant radio pulses. In addition, we measure IP and LFP pulse phases relative to the MP that are consistent with recent measurements, which have shown that the phases of these pulse components are evolving with time.

Subject headings: neutron stars: general — pulsars: individual — Crab pulsar (PSR B0531+21) — polarization

1. Introduction

The Australia Telescope National Facility Pulsar Catalog (Manchester et al. 2005) lists over 2300 radio pulsars. Several radio studies (e.g., Gould & Lyne 1998; Karastergiou & Johnston 2006; Weltevrede & Johnston 2008) have measured the polarization for many of these pulsars. Radio pulsars typically show moderate-to-strong linear polarization (P), being stronger for those of higher spin-down energy-loss rate (Weltevrede & Johnston 2008, Figure 8). The linear polarization sometimes exhibits a characteristic swing or sweep of the position angle in an S-like shape near the pulse center, which is routinely interpreted in terms of the rotating vector model (RVM, Radhakrishnan & Cooke 1969). For this model the point of emission is assumed to be in the polar cap region of the pulsar where a dipolar magnetic-field line points with a small angle (beamwidth) towards the observer. The two free parameters of this simple model are the angle between the axes of rotation and the orientation of the magnetic dipole, and the view angle between the line of sight and the rotation axis. The variation of the radio position angle from some pulsars (e.g., Lyne & Graham-Smith 2006, and references therein) can be described by this model.

The Crab pulsar, the compact remnant of SN1054, and its pulsar wind nebula (PWN) are amongst the most intensively studied objects in the sky. The pulsar is one of the youngest and most energetic and its pulsed emission has been detected from 10 MHz (Bridle 1970) up to 400 GeV by VERITAS (Aliu et al. 2011) and by MAGIC (Aleksić et al. 2012). The PWN is detected at energies up to 100 TeV (Aharonian et al. 2004, 2006; Allen & Yodh 2007; Abdo et al. 2012). Both the pulsar and nebula are predominantly sources of non-thermal radiation (synchrotron, curvature, and Compton processes), indicated not only by the broadband spectral continua but also by strong polarization in many wavelength bands (Lyne & Graham-Smith 2006; Bühler & Blandford 2013).

In the visible band, spatially-resolved polarimetry of the nebula, which began over a half century ago (Oort & Walraven 1956; Woltjer 1957), continues (e.g., Moran et al. 2013,

and references therein). Owing to its brightness, phase-resolved optical polarimetry of the pulsar has also been possible (Jones et al. 1981; Smith et al. 1988; Słowińska et al. 2009). However, phase-resolved X- and γ -ray polarimetry measurements of the Crab pulsar require space-based instruments, which have had limited sensitivity. OSO-8 observations (Silver et al. 1978) of the Crab established only upper limits to the X-ray (2.6-keV and 5.2-keV) polarization of the pulsed emission. INTEGRAL IBIS observations (Forot et al. 2008; Moran et al. 2014) also detect no significant pulsed γ -ray (200–800-keV) polarization, although the off-pulse emission appears highly linearly polarized and probably associated with structures close to the pulsar rather than with the pulsar itself.

The Crab pulsar’s light curve exhibits different features at different wavelengths but it is currently the only pulsar for which the principal features in the light curve persist over all wavelengths, from radio to γ -rays. There are two principal components—the main pulse (MP) and the interpulse (IP). This double-peak structure remains more-or-less phase-aligned over all spectral bands (Moffett & Hankins 1996; Kuiper et al. 2001). One of several additional features in the radio band is the low-frequency precursor (LFP, e.g., Moffett & Hankins 1996; 1999) or component, having very low amplitude and occurring ≈ 0.10 fractional pulse phase before the MP.

Manchester (1971) measured the linear polarization of the Crab pulsar’s MP and LFP components at two radio frequencies. The 0.410 GHz measurements found the MP to be 20% linearly polarized at position angle 140° and the LFP to be 80% linearly polarized at position angle 140° . The 1.664 GHz measurements found the MP to be 24% linearly polarized at position angle 60° and the LFP to be completely absent. As these measurements had rather large uncertainties and were obtained with a time resolution $1/256$ of the pulse period, they were quite limited for detecting variation of the linear polarization degree or position angle within a feature. However, Manchester noted a suggestion of rotation of the 1.664-GHz polarization position angle by about 30° through the MP.

More recently, Moffett & Hankins (1999) examined the pulse-profile morphology and polarization properties at three radio frequencies—1.424 GHz, 4.885 GHz, and 8.435 GHz—with a time resolution of $256 \mu\text{s}$ (about $1/130$ of the pulse period). The 1.424 GHz measurements found the MP to be 25% linearly polarized at position angle 120° ; the IP, 20% at position angle 120° ; and the LFP, 45% at position angle 155° . Moffett & Hankins note that the polarization position angle “changes across the full period, although not significantly within components”.

Here we first report our observations (§2), using the Westerbork Synthesis Radio Telescope (WSRT) in the Netherlands, of the full (linear and circular) 1.38-GHz polarization of the Crab pulsar, at high time resolution. We then describe the polarimetry analysis and

results (§3 and Appendix A) for the three pulse components, with a primary objective of determining the sweep of the position angle across each. Next we discuss the implications (§4) of our measurements and analysis upon theoretical models for the pulsar emission. Finally, we summarize our conclusions (§5).

2. The Observations

The WSRT observations were conducted on 2011 August 8, using 14 25-m-diameter dishes, which are combined coherently for pulsar observations, to form the equivalent of a 94-m dish. To combine coherently the dishes, correlated data from observation of a bright calibrator source is used to determine phase delays between dishes. This is initially done using an unpolarized calibration source to determine the delays between the two linear polarizations separately, and is followed by an observation of a polarized calibrator to determine any residual delays between the two polarizations. The interferometric nature of the WSRT means that it partially resolves out the radio-bright Nebula, thus improving sensitivity over typical single-dish observations. Moreover the WSRT is an equatorially mounted telescope, so there is no need to correct for parallactic angle.

The PuMa-II (Karuppusamy et al. 2008) pulsar back-end was used to record Nyquist-sampled voltages at a resolution of 8 bits, across a bandwidth of 160 MHz at a central frequency of 1380 MHz, for PSRs B0531+21 (Crab) and for B0355+54, for a total of 144 and 18 minutes, respectively. The data were subsequently coherently de-dispersed and folded using the DSPSR (van Straten & Bailes 2011) software package. Polarization profiles were formed after correcting for (frequency-dependent) interstellar Faraday rotation (rotation measure $RM = -42.3 \pm 0.5 \text{ rad m}^{-2}$) of the position angle, using the PSRCHIVE software package (van Straten et al. 2012). The polarization calibration was already carried out when forming the coherent sum of the dishes, nevertheless PSR B0355+54 was observed to verify that no further polarization calibration was required. Comparison with the profile observed by Gould & Lyne (1998) showed that the polarization calibration matched exactly. The Crab-pulsar profile was folded using the Jodrell Bank Ephemeris¹ with 8192 bins (about 4.1 $\mu\text{s}/\text{bin}$) across the pulse profile, matching the time resolution of the data after filter-banking and coherent de-dispersion. This time resolution was chosen also to match approximately broadening caused by scattering of the Crab pulsed emission by free electrons in the Crab Nebula.

Figure 1 displays our measurement of the four Stokes parameters I , Q , U , and V —

¹<http://www.jb.man.ac.uk/pulsar/crab.html>

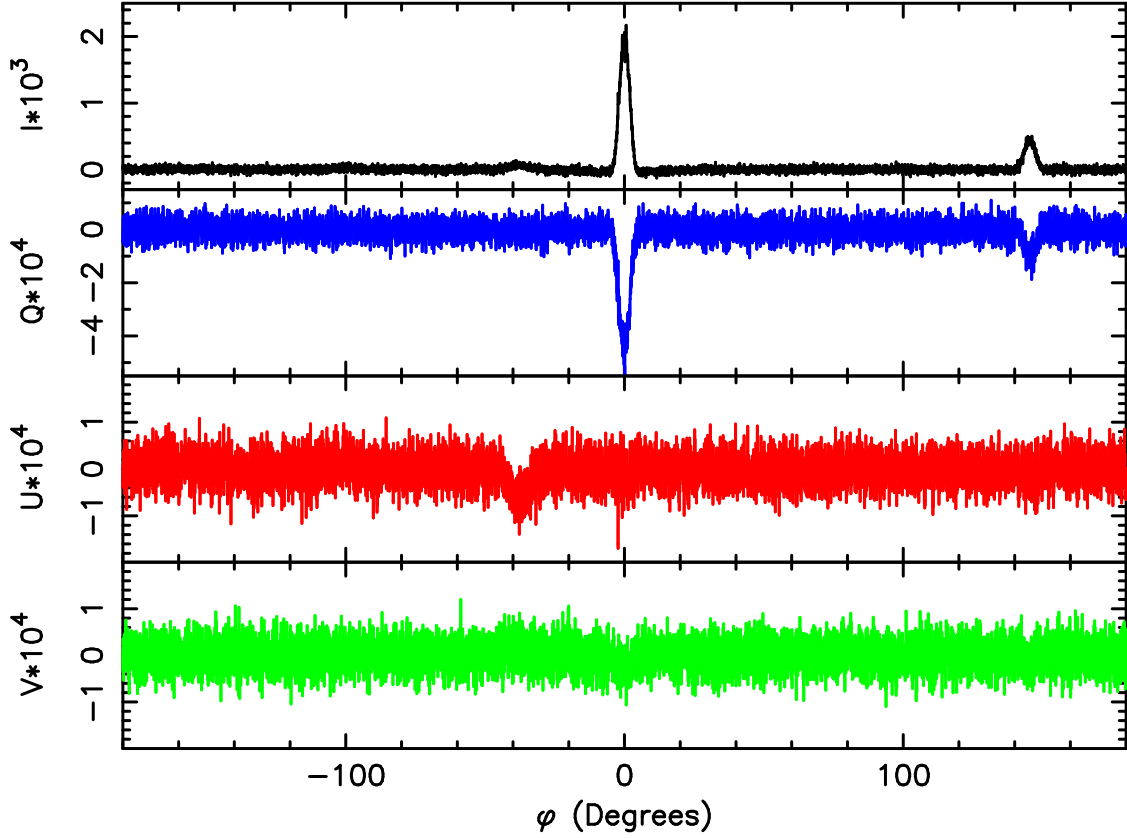


Fig. 1.— Four Stokes parameters $I \times 10^3$, $Q \times 10^4$, $U \times 10^4$, and $V \times 10^4$ (arbitrary units) as functions of pulse phase φ , where the peak of the main pulse (MP) defines $\varphi = 0$. The coordinate system for the Stokes parameters here sets $U = 0$ and $Q < 0$ for the MP.

which fully characterize the polarization—folded on the pulse period. Unfortunately, we were unable to determine the absolute polarization position angle for the Crab pulsar observation. Instead, we selected a coordinate system for the Stokes parameters such that the MP has $U = 0$ and $Q < 0$. Inspection of Figure 1 immediately shows that our 1.38-GHz observations detect the flux and polarization of three components—MP, IP, and LFP. Like the MP, the IP has $U \approx 0$ and $Q < 0$; but the LFP has $U < 0$ and $Q \approx 0$: Thus, the polarization position angles for the MP and the IP are roughly equal but differ from that of the LFP by about 40° (cf. Eq. 2). Similarly, but less obviously, the circular polarization of the MP and the IP are comparable, but that of the LFP has opposite polarity.

3. Analysis and Results

While the Stokes parameters have the virtue that they are statistically independent, the more intuitive parameters are the linear-polarization degree p_L (Eq. 1) and position angle ψ (Eq. 2), and the circular-polarization (signed) degree p_C (Eq. 3):

$$p_L = \sqrt{(Q^2 + U^2)}/I; \quad (1)$$

$$\psi = \frac{1}{2} \tan^{-1}(U/Q); \quad (2)$$

$$p_C = V/I. \quad (3)$$

For the MP, we estimate $p_L(\varphi)$, $\psi(\varphi)$, and $p_C(\varphi)$ by directly applying Equations 1, 2, and 3 to the measured I , Q , U , and V over the main pulse.

Figures 2, 3, and 4 display the direct estimates of $p_L(\varphi)$, $\psi(\varphi)$, and $p_C(\varphi)$, respectively, over the MP. The MP is about 24% linearly polarized at approximately 90° position angle with respect to the adopted coordinate system; it is about -1.5% circularly polarized (i.e., left-handed). Neither $p_L(\varphi)$, $\psi(\varphi)$, nor $p_C(\varphi)$ exhibits any obvious variation through the pulse. The increasingly large excursions near the extremes of the plot ranges result from the low-signal-to-noise ratio in the wings of the pulse. In order to deal effectively with low-signal-to-noise data in the wings of the MP and throughout the weaker pulses, especially the LFP, we adopt a more rigorous forward-modeling approach to fit the measured Stokes data to the modeled $I(\varphi)$, $Q(\varphi)$, $U(\varphi)$, and $V(\varphi)$:

$$Q(\varphi) = I(\varphi)p_L(\varphi) \cos(2\psi(\varphi)); \quad (4)$$

$$U(\varphi) = I(\varphi)p_L(\varphi) \sin(2\psi(\varphi)); \quad (5)$$

$$V(\varphi) = I(\varphi)p_C(\varphi). \quad (6)$$

Appendix A describes in some detail our approach for fitting polarization models to the Stokes data. As Figures 2, 3, and 4 indicate that neither $p_L(\varphi)$, $\psi(\varphi)$, nor $p_C(\varphi)$ varies rapidly across the pulse profile (at least for the MP), the approach simply models $p_L(\varphi)$, $\psi(\varphi)$, and $p_C(\varphi)$ as Taylor-series expansions in the phase-angle offset $\Delta\varphi \equiv (\varphi - \varphi_0)$ from the center φ_0 of the respective pulse feature (MP, IP, or LFP). Table 1 tabulates the best-fit Taylor-expansion coefficients for the polarization dependence upon phase-angle offset:

$$p_L(\varphi) = p_{L0} + p'_{L0}(\varphi - \varphi_0) + \frac{1}{2}p''_{L0}(\varphi - \varphi_0)^2; \quad (7)$$

$$\psi(\varphi) = \psi_0 + \psi'_0(\varphi - \varphi_0) + \frac{1}{2}\psi''_0(\varphi - \varphi_0)^2; \quad (8)$$

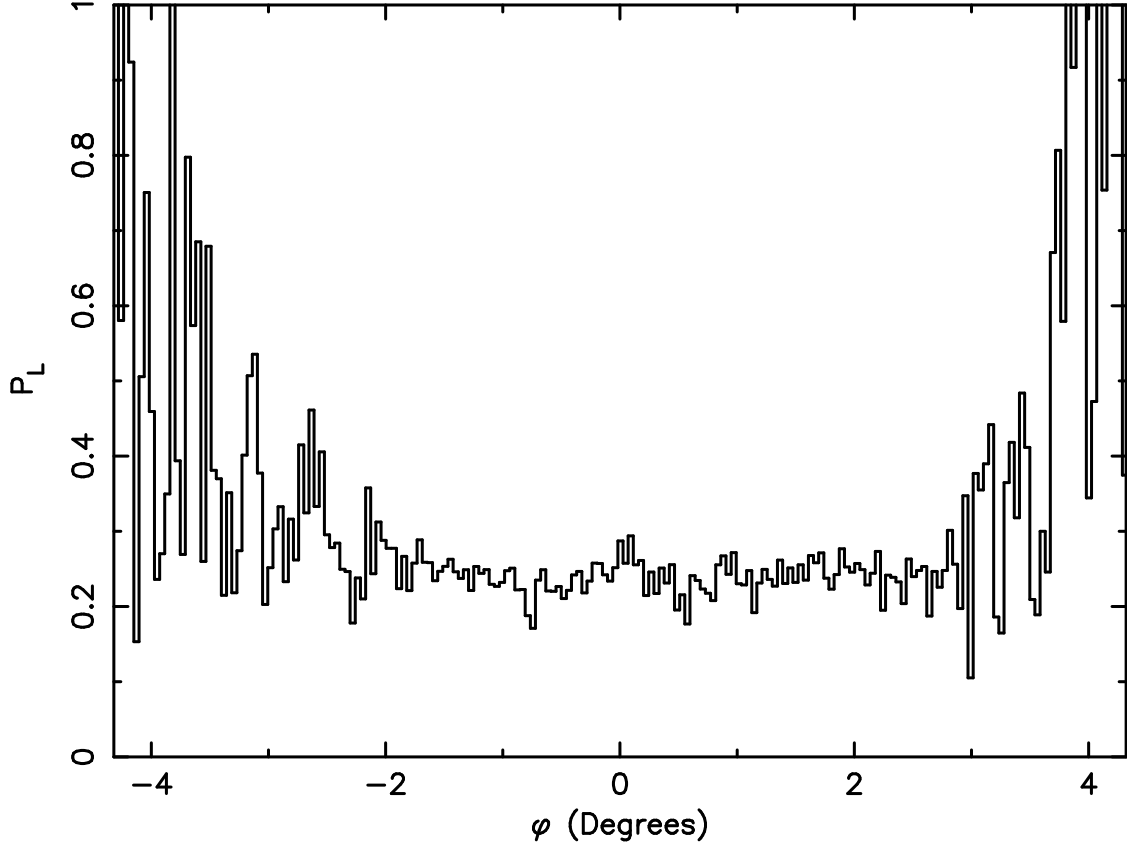


Fig. 2.— Direct estimate of the fractional linear polarization p_L over the MP, as a function of pulse phase φ . The degree of linear polarization is $p_L \approx 24\%$ and does not change perceptibly over the central 5° of pulse phase. NB: Behavior near the extremes of the plot range is an artifact of low signal-to-noise ratio in the wings of the pulse.

$$p_C(\varphi) = p_{C0} + p'_{C0}(\varphi - \varphi_0) + \frac{1}{2}p''_{C0}(\varphi - \varphi_0)^2. \quad (9)$$

An important conclusion of this study is that the the Stokes data are consistent—within statistical uncertainties—with constant polarization position angle ψ across each of the three pulse features (MP, IP, and LFP) individually. However, the MP does exhibit a small but statistically significant quadratic variation in the linear-polarization degree p_L . While our 1.380-GHz polarimetry of the Crab pulsar has finer time resolution and better statistical accuracy than previous 1.424-GHz polarimetry (Moffett & Hankins 1999), measured values for the polarization degree and position angle (relative to MP) are mostly similar for the MP and for the IP. The only significant difference is for the LFP’s linear polarization degree and position angle. We measured nearly total ($98\% \pm 6\%$) linear polarization at a $+40.8^\circ \pm 1.5^\circ$

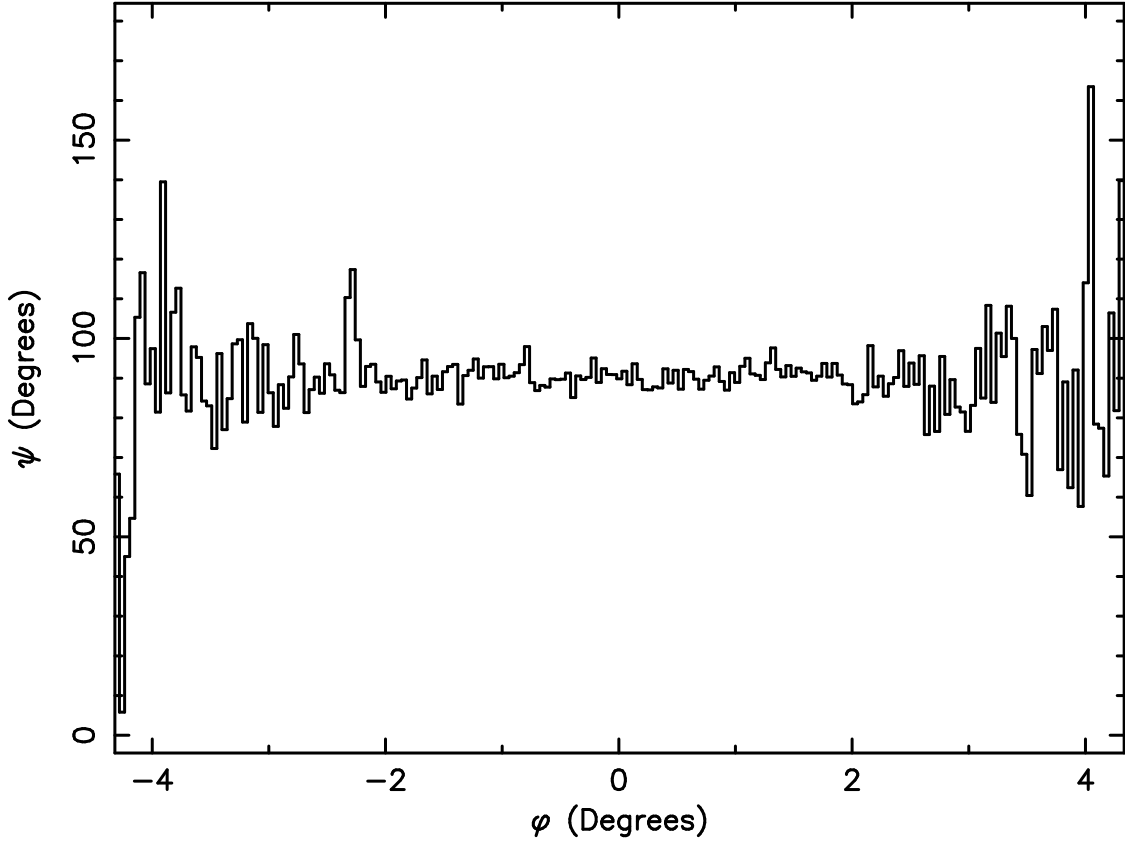


Fig. 3.— Direct estimate of the relative polarization position angle ψ over the MP, as a function of pulse phase φ . The (relative) polarization position angle is $\psi \approx 90^\circ$ and does not change perceptibly over the central 5° of pulse phase. NB: Behavior near the extremes of the plot range is an artifact of low signal-to-noise ratio in the wings of the pulse.

position-angle offset from the MP, whereas Moffett & Hankins (1999) found the LFP to be $\approx 40\%$ linearly polarized at a $\approx +30^\circ$ position-angle offset from the MP. We also detect circular polarization, which is moderately strong in the LFP ($20.5 \pm 4.9\%$) but weak and opposite polarity in the MP ($-1.3\% \pm 0.2\%$) and in the IP ($-3.2\% \pm 0.9\%$). In contrast with Moffett & Hankins, we find no significant variation in the circular polarization across any of the three pulse components MP, IP, and LFP.

Another important conclusion—albeit peripheral to the polarimetry—relates to substructure in the pulse profile of the MP. The fine time resolution and better statistical accuracy of our radio observation of the Crab pulsar resulted in measurement of statistically significant substructure (Appendix A.3) in the profile of the main pulse (Figure 5). The typical width of the substructure is roughly $10 \mu\text{s}$ —i.e., ≤ 0.1 the width of the MP profile. As

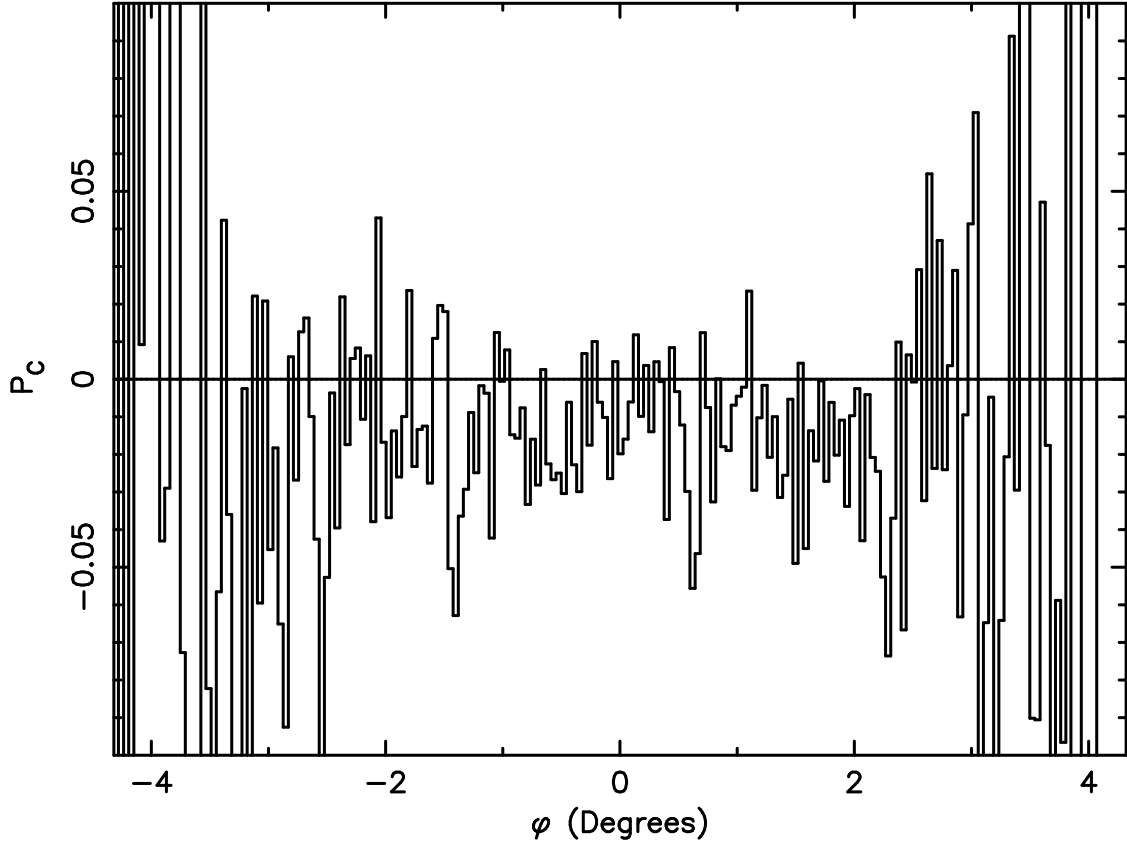


Fig. 4.— Direct estimate of the fractional circular polarization p_C over the MP, as a function of pulse phase φ . The degree of circular polarization is $p_C \approx -1.5\%$ (i.e., left-handed) and does not change perceptibly over the central 5° of pulse phase. NB: Behavior near the extremes of the plot range is an artifact of low signal-to-noise ratio in the wings of the pulse.

the current analysis utilizes the sum of all data collected during the observation at a single epoch (2011 August 8), we have not assessed the temporal behavior of the profile. However, we presume that this substructure results from sporadic giant radio pulses (Bhat et al. 2008; Karuppusamy et al. 2010; Majid et al. 2011; Hankins et al. 2003) occurring during the 144-minute observation. Note that, although the substructure is readily apparent in the I profile of the MP, the subpulses contribute only about 5% of the fluence in the MP over the observation.

We also note that our WSRT-measured pulse-phase offsets of the IP and of the LFP from the MP are in good agreement with contemporaneous measurements at Jodrell Bank (Lyne et al. 2013). This tends to support the conclusion of Lyne et al. (2013) that the phase

Table 1: Best-fit polarization coefficients for the MP, IP, and LFP, using a single Gaussian for each pulse profile and up-to-quadratic variations in polarization functions $p_L(\varphi)$, $\psi(\varphi)$, and $p_C(\varphi)$.

Parameter	Units	MP	IP	LFP
$\varphi_0 - \varphi_{\text{MP}}$	$^\circ$	$\equiv 0$	145.390 ± 0.027	-37.74 ± 0.19
p_{L0}	%	23.17 ± 0.31	21.3 ± 1.0	98.2 ± 6.7
p'_{L0}	%/ $^\circ$	-0.32 ± 0.20	1.02 ± 0.62	-0.8 ± 2.2
p''_{L0}	%/ $^\circ$ / $^\circ$	1.25 ± 0.24	-0.02 ± 0.63	0.0 ± 1.3
$\psi_0 - \psi_{\text{MP}}$	$^\circ\text{PA}$	$\equiv 0$	-0.1 ± 1.3	40.8 ± 1.5
ψ'_0	$^\circ\text{PA}/^\circ$	-0.16 ± 0.20	0.82 ± 0.78	-0.16 ± 0.49
ψ''_0	$^\circ\text{PA}/^\circ$ / $^\circ$	-0.06 ± 0.21	1.00 ± 0.89	-0.21 ± 0.28
p_{C0}	%	-1.25 ± 0.21	-3.15 ± 0.94	20.5 ± 4.9
p'_{C0}	%/ $^\circ$	0.01 ± 0.14	0.38 ± 0.56	0.3 ± 1.7
p''_{C0}	%/ $^\circ$ / $^\circ$	-0.23 ± 0.16	0.47 ± 0.57	-0.49 ± 0.97

separations of the IP and of the LFP from the MP are evolving with time. Furthermore, the evolution of phase separations might contribute to the difference between our measurement of the LFP’s polarization and earlier measurements (Moffett & Hankins 1999).

4. Implications for Theoretical Models

The MP and IP appear at roughly the same pulse phase from radio to γ -ray wavelengths, suggesting that their emission originates from a similar location in the magnetosphere at all wavebands. Modeling of γ -ray light curves from the many pulsars observed by the *Fermi Gamma-ray Space Telescope* (Abdo et al. 2013) strongly indicates that the high-energy emission originates in the outer magnetosphere, at altitudes comparable to the light cylinder radius (Romani & Watters 2010; Pierbattista et al. 2013). Outer magnetosphere emission models, such as the outer gap (Romani & Yadigaroglu 1995), slot gap (Muslimov & Harding 2004), and current sheet (Pétri & Kirk 2005) had been proposed and studied prior to the *Fermi* observations, but their emission geometry seems to account for the characteristics and variety of observed γ -ray light curves. In addition, *Fermi* has discovered a number of γ -ray millisecond pulsars whose radio peaks, like the Crab pulsar, are nearly aligned with their γ -ray peaks (e.g., Espinoza et al. 2013). Modeling both the γ -ray and radio light curves of these pulsars with the same outer magnetosphere emission models used to model young pulsars

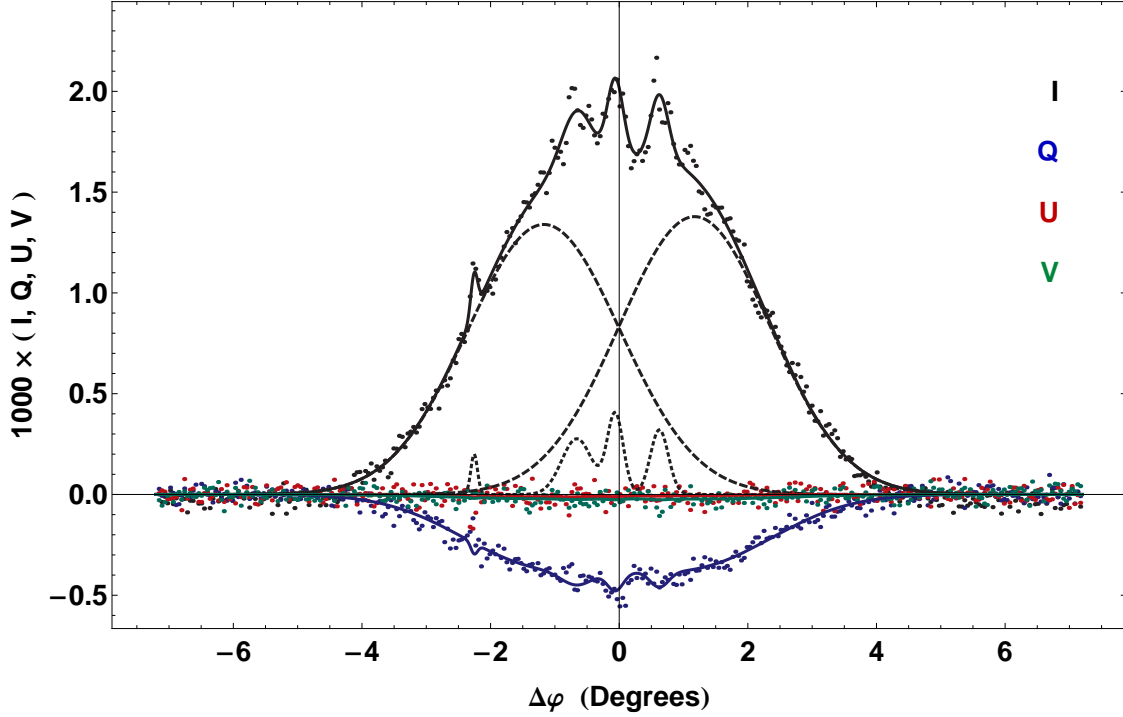


Fig. 5.— Stokes data I , Q , U , and V versus pulse phase offset $\Delta\varphi$ from the center of the main pulse (MP). The lines represent the best-fit (minimum- χ^2) Stokes functions for a multi-Gaussian profile and up-to-second-order variations in liner-polarization degree, position angle, and circular-polarization degree. The pulse profile comprises 2 broad and 4 narrow Gaussians.

has suggested that their radio emission may originate from very high altitudes (Venter et al. 2012).

Emission at altitudes comparable to the light-cylinder radius produce caustic peaks, formed by cancellation of the phase differences due to aberration and retardation with that due to the field-line curvature of radiation along the trailing magnetic-field lines. In the outer magnetosphere models, the peaks in the light curves form when the observer’s sight line sweeps across one or more of the bright caustics. The caustics display distinct linear polarization characteristics (Dyks & Rudak 2003), including fast sweeps of the position angle and dips in polarization degree at the peaks, which are caused by the piling up of the radiation emitted at a large range of altitudes and magnetic-field directions into the caustics. These characteristics are in fact seen in the optical polarization of the Crab pulsar (Słowińska et al. 2009), which exhibits rapid swings of the position angle across both the MP and IP, as well as dips in polarization degree to the 5% level on the trailing edge of each

peak.

From the results presented in this paper, however, the characteristics of the radio linear polarization of the MP and IP resemble neither those of caustics in existing geometric models nor those observed in the optical emission. The lack of position-angle swing in the radio MP and IP is in stark contrast to the rapid position-angle swings of the optical. The very low circular polarization and moderate linear polarization observed here in the radio MP and IP are consistent with caustics, but the observed linear-polarization values ($\approx 22\%$) in the radio are significantly higher than those of the optical, and there is only a small variation with phase in the MP. On the other hand, the radio pulses are much narrower than the optical pulses, indicating that the radio MP and IP may originate along a smaller range of altitudes and/or subset of field lines. We used the method of Dyks et al. (2004) to model linear-polarization degree p_L and position angle ψ for smaller ranges of altitude and smaller gap widths than in standard slot-gap or outer-gap models. Although these model ranges produce narrower caustic peaks with less position-angle swing and depolarization, it is difficult to produce both $\psi(\varphi)$ and $p_L(\varphi)$ curves with no variation at the peaks. We modeled the emission using both retarded-vacuum-dipole (Deutsch 1955) and force-free (Contopoulos & Kalapotharakos 2010) magnetic-field geometries. While the force-free geometry, whose poloidal field lines are straighter than those in vacuum, can give a flat position angle ($\psi'(\varphi) \approx 0$) for certain inclination and viewing angles, the model's p_L shows strong variation across the peaks in contradiction with the data.

It is possible that the radio linear polarization in the MP and LP is very sensitive to the magnetic-field structure. Existing models explored only the two extremes of vacuum (with accelerating fields but no plasma) and force-free (with plasma but no accelerating fields), neither of which describe real pulsars. More realistic, dissipative magnetosphere models with finite conductivity now exist (Kalapotharakos et al. 2012; Li et al. 2012) and should be used to model light curves and polarization characteristics. It is also possible that the radio emission in the MP and IP occurs along sets of field lines that lie deeper within the open/closed field boundary or the current sheet and have different polarization properties.

The low-frequency precursor (LFP) is substantially weaker than the MP and IP at 1.4 GHz. As its name suggests, the LFP is not detected at radio frequencies higher than a few GHz and has no corresponding component in the visible band. The nearly complete radio polarization ($p_L \approx 98\%$ and $p_C \approx 20\%$) of the LFP support the hypothesis that it is a highly coherent, low-altitude core component.

5. Conclusions

Our 1.38-GHz observations of the Crab pulsar measured significant linear and circular polarization in the three most prominent pulse components—the main pulse (MP), inter pulse (IP), and low-frequency precursor (LFP). These results are mostly in agreement with previous measurements of linear polarization at similar radio frequencies (cf. Moffett & Hankins 1999). The MP and IP are moderately linearly polarized ($p_L \approx 24\%$ and 21% , respectively) at the same position angle ($\psi_{\text{IP}} - \psi_{\text{MP}} \approx 0$); they are weakly circularly polarized ($p_C \approx -1.3\%$ and -3.2% , respectively). In contrast, the LFP is very strongly linearly polarized ($p_L \approx 98\%$), at a position angle $+40^\circ$ from that of the MP or IP, and moderately circularly polarized ($p_C \approx 20\%$).

The fine time resolution (Period/8192 = $4.1 \mu\text{s}$) and good sensitivity of the measurements at the Westerbork Synthesis Radio Telescope (WSRT) enabled a meaningful search for changes in linear-polarization degree p_L , in position angle ψ , and in circular-polarization degree p_C across each of the three pulse components. Neither the MP, IP, nor LFP exhibits a statistically significant change in the polarization position angle or circular polarization across the pulse. For the MP, the linear term (“sweep”) is well constrained: $\psi'_{0\text{MP}} = (-0.16 \pm 0.20)^\circ\text{PA}/^\circ$. Likewise, neither the IP nor LFP displays a statistically significant change in the polarization degree. However, the MP does show a small but statistically significant quadratic variation in linear-polarization degree— $p''_{L0\text{MP}} = (1.25 \pm 0.24)\%/^\circ/^\circ$ about its central value— $p_{L0\text{MP}} = (23.2 \pm 0.3)\%$ —for a pulse-average linear polarization $\bar{p}_{L\text{MP}} = (24.1 \pm 0.3)\%$.

The lack of strong sweeps in position angle contrasts with the rapid swings observed in the visible band. Current models for pulsar emission geometries do not readily account for the absence of substantial variations in both polarization degree and position angle across a pulse component. Thus, alternative models—e.g., dissipative magnetospheres—should be considered in modeling the radio polarization of the Crab pulsar’s MP and IP. The nearly complete polarization of the LFP suggest that it originates at a different location and via a different mechanism than do the stronger MP and IP.

Finally, the fine time resolution and high signal-to-noise ratio in the MP data led to detection of statistically significant substructure in its pulse profile. We surmise that this substructure results from giant radio pulses occurring during the 144-minute observation.

The Westerbork Synthesis Radio Telescope (WSRT) is operated by ASTRON, the Netherlands Institute for Radio Astronomy, with support from NWO, the Netherlands Foundation for Scientific Research. AS acknowledges grant DEC-2011/03/D/ST9/00656 from

the Polish National Science Centre; BWS, a Consolidated Grant from the UK Science and Technology Facilities Council; AKH, NASA grants Astrophysics Theory 12-ATP12-0169 and Fermi Guest Investigator 11-FERMI11-0052; AJvdH, Advanced Investigator Grant 247295 (PI: R. A. M. J. Wijers) from the European Research Council; and SLO, RFE and MCW, support by NASA’s Chandra Program.

A. Statistical analysis

A.1. Procedures

As Figure 1 shows, the main pulse (MP), interpulse (IP), and low-frequency precursor (LFP) are well separated in the 1.38-GHz data folded on the Crab pulsar’s period. Consequently, we choose to analyze each of these three features individually, using phase ranges $(-7.2^\circ, 7.2^\circ)$ for the MP, $(134.6^\circ, 156.2^\circ)$ for the IP, and $(-52.1^\circ, -23.3^\circ)$ for the LFP, where the center of the MP defines pulse-phase angle $\varphi = 0^\circ$. We use data over the remaining phase ranges to measure the off-pulse mean and the root-of-mean-square (RMS) noise in I , Q , U , and V . For convenience, we pre-process the raw data by subtracting the respective off-pulse mean value, under the assumption that the expectation values for I , Q , U , and V are zero away from pulse features. Furthermore, we take the RMS noise levels as estimators of the statistical standard deviations σ_I , σ_Q , σ_U , and σ_V .

In order to fit the model to the data for each pulse feature, we minimize the chi-square statistic of the combined Stokes data

$$\chi^2(\varpi) = \chi_I^2(\varpi) + \chi_Q^2(\varpi) + \chi_U^2(\varpi) + \chi_V^2(\varpi) = \sum_{n=1}^N \left[\frac{(I_n - I(\varphi_n; \varpi))^2}{\sigma_I^2} + \frac{(Q_n - Q(\varphi_n; \varpi))^2}{\sigma_Q^2} + \frac{(U_n - U(\varphi_n; \varpi))^2}{\sigma_U^2} + \frac{(V_n - V(\varphi_n; \varpi))^2}{\sigma_V^2} \right], \quad (\text{A1})$$

with respect to a set ϖ of K model parameters, leaving $\nu = N - K$ degrees of freedom. We obtain the statistical uncertainty in each parameter, based upon $\Delta\chi^2 = \chi^2 - \chi_{\min}^2$. To perform the χ^2 analysis, we used the *Mathematica*TM (Wolfram 2013) function `NonlinearModelFit`², which finds the best-fit model parameters, their errors, the correlation matrix amongst them, etc.

Modeling the Stokes data requires parameterized functions for the pulse profile $I(\varphi)$, the linear-polarization fraction $p_L(\varphi)$, the polarization position angle $\psi(\varphi)$, and the circular-polarization fraction $p_C(\varphi)$ (cf. Equations 4, 5, and 6 for $Q(\varphi)$, $U(\varphi)$, and $V(\varphi)$, respectively).

²<http://reference.wolfram.com/mathematica/ref/NonlinearModelFit.html>

As there is no evidence for rapid changes in polarization degree or position angle over a pulse feature (cf. Figures 2, 3, and 4), simple Taylor-series expansions suffice:

$$\begin{aligned} p_L(\varphi) &= p_L(\varphi_0) + p'_L(\varphi_0)(\varphi - \varphi_0) + \frac{1}{2}p''_L(\varphi_0)(\varphi - \varphi_0)^2 + \dots \\ &\equiv p_{L0} + p'_{L0}(\varphi - \varphi_0) + \frac{1}{2}p''_{L0}(\varphi - \varphi_0)^2 + \dots; \end{aligned} \quad (\text{A2})$$

$$\begin{aligned} \psi(\varphi) &= \psi(\varphi_0) + \psi'(\varphi_0)(\varphi - \varphi_0) + \frac{1}{2}\psi''(\varphi_0)(\varphi - \varphi_0)^2 + \dots \\ &\equiv \psi_0 + \psi'_0(\varphi - \varphi_0) + \frac{1}{2}\psi''_0(\varphi - \varphi_0)^2 + \dots; \end{aligned} \quad (\text{A3})$$

$$\begin{aligned} p_C(\varphi) &= p_C(\varphi_0) + p'_C(\varphi_0)(\varphi - \varphi_0) + \frac{1}{2}p''_C(\varphi_0)(\varphi - \varphi_0)^2 + \dots \\ &\equiv p_{C0} + p'_{C0}(\varphi - \varphi_0) + \frac{1}{2}p''_{C0}(\varphi - \varphi_0)^2 + \dots. \end{aligned} \quad (\text{A4})$$

To parameterize the pulse profile, we use a Gaussian (§A.2) for each pulse feature (MP, IP, or LFP) or multiple Gaussians (§A.3) for the MP.

A.2. Single-Gaussian fits to the MP, the IP, and to the LFP

To complete the parameterized model for the four Stokes functions, we assume a Gaussian profile:

$$I(\varphi) = I_0 \exp\left(-\frac{(\varphi - \varphi_0)^2}{2\sigma_\varphi^2}\right), \quad (\text{A5})$$

with I_0 the value of $I(\varphi)$ at pulse center, σ_φ the Gaussian width, and φ_0 the phase at the pulse center. Combining this parameterization with Equations 4, 5, 6, A2, A3, A4, the full model for the other three Stokes functions follows:

$$\begin{aligned} Q(\varphi) &= I_0 \exp\left(-\frac{(\varphi - \varphi_0)^2}{2\sigma_\varphi^2}\right) [p_{L0} + p'_{L0}(\varphi - \varphi_0) + \frac{1}{2}p''_{L0}(\varphi - \varphi_0)^2] \\ &\quad \times \cos(2[\psi_0 + \psi'_0(\varphi - \varphi_0) + \frac{1}{2}\psi''_0(\varphi - \varphi_0)^2]); \end{aligned} \quad (\text{A6})$$

$$\begin{aligned} U(\varphi) &= I_0 \exp\left(-\frac{(\varphi - \varphi_0)^2}{2\sigma_\varphi^2}\right) [p_{L0} + p'_{L0}(\varphi - \varphi_0) + \frac{1}{2}p''_{L0}(\varphi - \varphi_0)^2] \\ &\quad \times \sin(2[\psi_0 + \psi'_0(\varphi - \varphi_0) + \frac{1}{2}\psi''_0(\varphi - \varphi_0)^2]); \end{aligned} \quad (\text{A7})$$

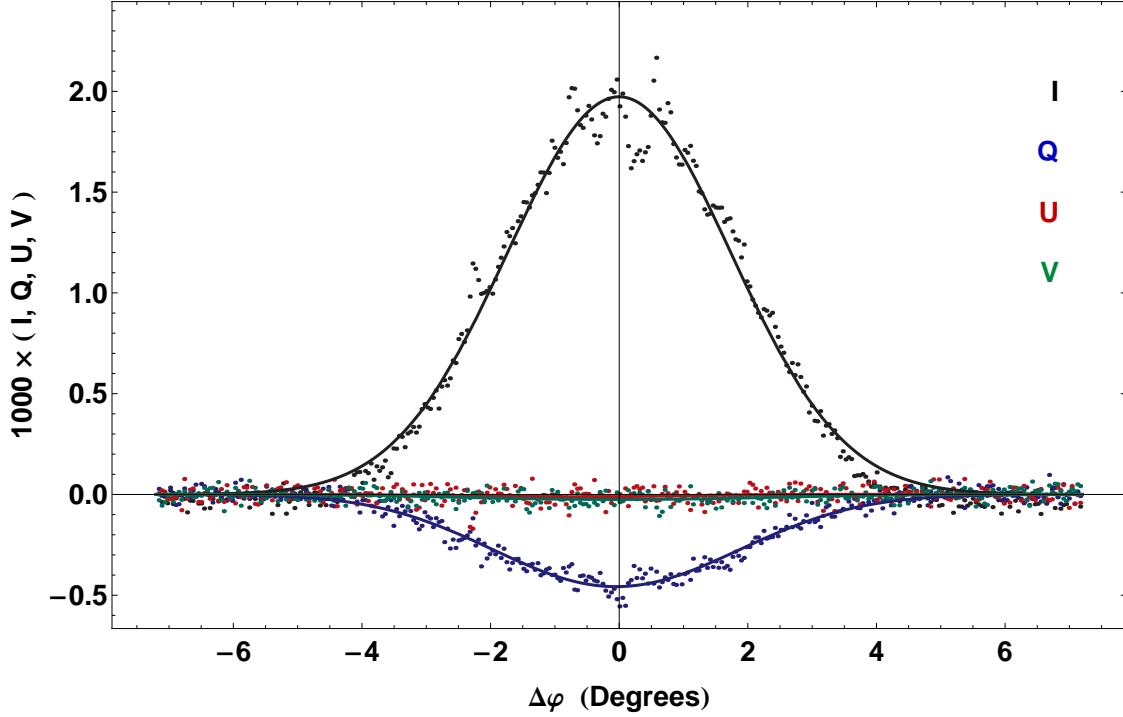


Fig. 6.— Stokes data I , Q , U , and V versus pulse phase offset $\Delta\varphi$ from the center of the main pulse (MP). The lines represent the best-fit (minimum- χ^2) Stokes functions for a single-Gaussian profile and up-to-second-order variations in polarization degree and in position angle.

$$V(\varphi) = I_0 \exp\left(-\frac{(\varphi - \varphi_0)^2}{2\sigma_\varphi^2}\right) \left[p_{C0} + p'_{C0}(\varphi - \varphi_0) + \frac{1}{2}p''_{C0}(\varphi - \varphi_0)^2\right]. \quad (\text{A8})$$

Figures 6, 7, and 8 display the Stokes data for the MP, IP, and LFP, respectively. The lines represent the best-fit (minimum- χ^2) Stokes functions (Equations A5, A6, A7, and A8) for a single-Gaussian profile $I(\varphi)$ and up-to-quadratic variations in linear-polarization degree $p_L(\varphi)$, in position angle $\psi(\varphi)$, and in circular-polarization degree $p_C(\varphi)$. Tables 2, 3, and 4 tabulate the results of the χ^2 analysis for a Gaussian profile and retaining polarization terms (Equations A6, A7, and A8) through, zeroth, first, and second order, respectively. For each pulse feature—MP, IP, and LFP—the tables list the minimum χ^2 and degrees of freedom ν for I , Q , U , and V data sets combined and separately, followed by best-fit estimators and (1-sigma) uncertainties for the 3 pulse-profile parameters (I_0 , σ_φ , φ_0) and for the relevant polarization coefficients (p_{L0} , p'_{L0} , p''_{L0} ; ψ_0 , ψ'_0 , ψ''_0 ; p_{C0} , p'_{C0} , p''_{C0}). Note that these three tables reference the pulse-phase angles (φ_0) and polarization position angles (ψ_0) to the MP, as we set $\varphi_{\text{MP}} \equiv 0$ and were unable to obtain an absolute measurement of position angle

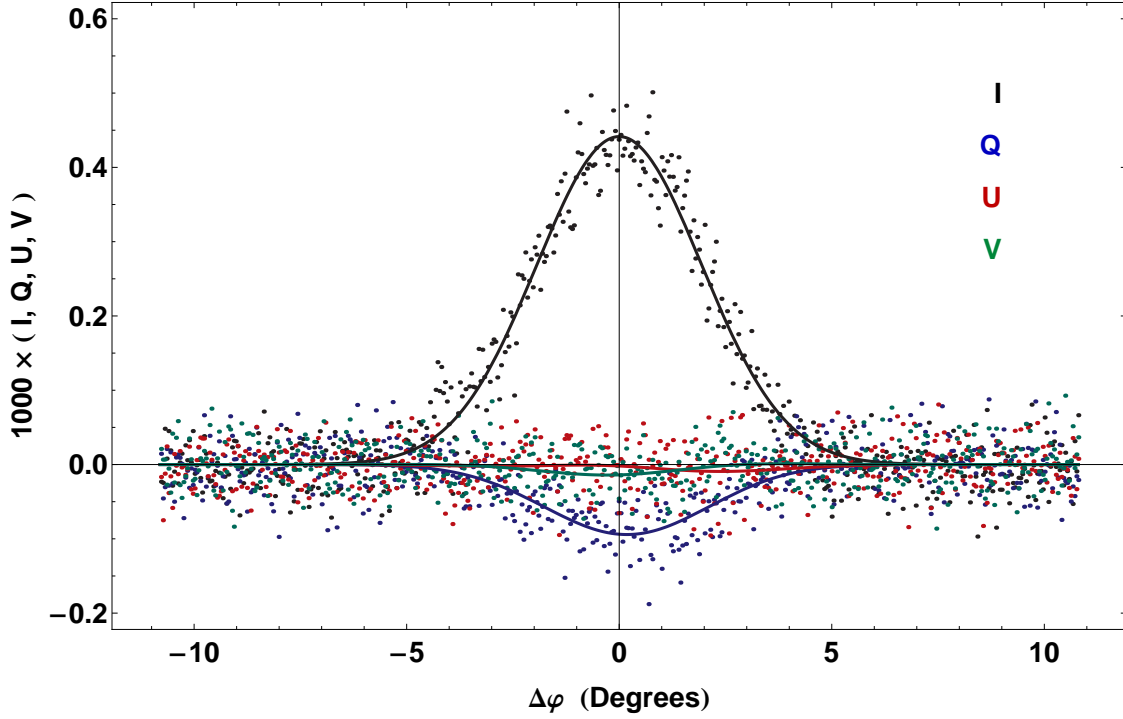


Fig. 7.— Stokes data I , Q , U , and V versus pulse phase offset $\Delta\varphi$ from the center of the inter pulse (IP). The lines represent the best-fit (minimum- χ^2) Stokes functions for a single-Gaussian profile and up-to-second-order variations in polarization degree and in position angle.

ψ_{MP} .

Table 3 documents that, to within statistical uncertainties, $p'_{L0} = 0$, $\psi'_0 = 0$, and $p'_{C0} = 0$ for each of the three pulse features—MP, IP, or LFP. Equivalently, including the three linear coefficients $p'_{L0} = 0$, $\psi'_0 = 0$, and $p'_{C0} = 0$, does not result in a statistically significant reduction in the value of χ^2_{min} (cf. Tables 2 and 3). In contrast, including the quadratic parameter p''_{L0} does significantly reduce the value of χ^2_{min} for the MP (cf. Table 4 with Table 3 or 2), but not for the IP nor for the LFP.

A.3. Comparison of model fits to MP

Table 2 shows that a single-Gaussian profile and constant polarization degree and position angle provide a statistically adequate fit to the Stokes data for the IP and for the LFP. However, the simple model does not provide a statistically adequate fit to the Stokes data

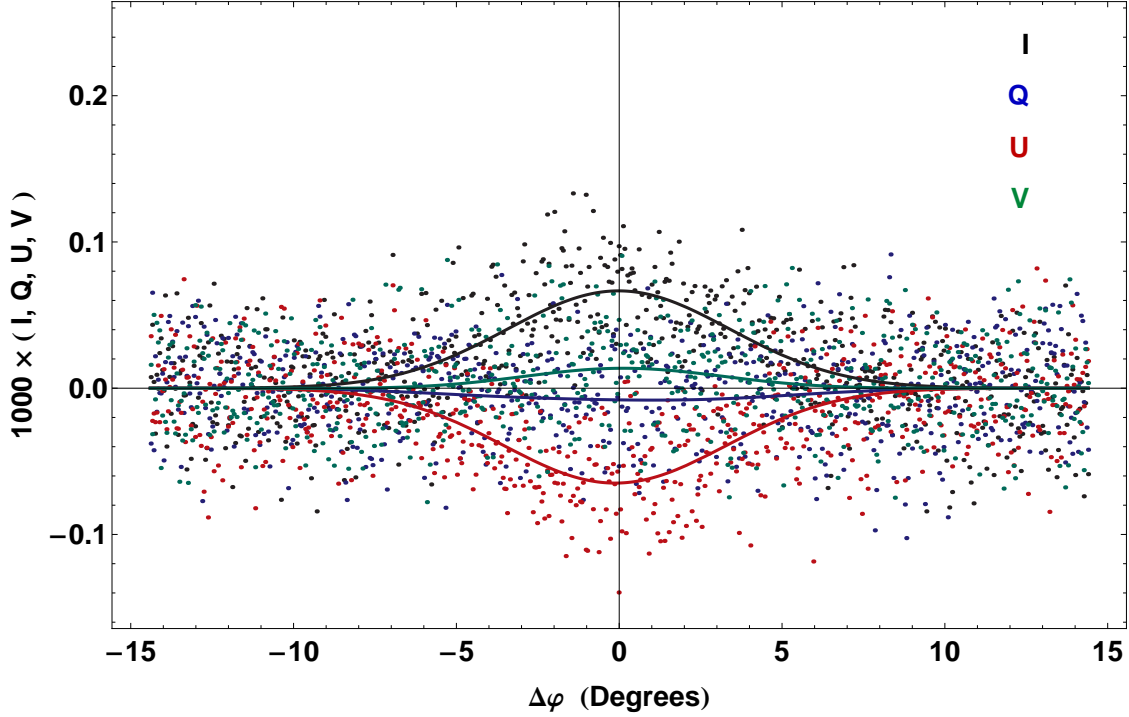


Fig. 8.— Stokes data I , Q , U , and V versus pulse phase offset $\Delta\varphi$ from the center of the low-frequency precursor (LFP). The lines represent the best-fit (minimum- χ^2) Stokes functions for a single-Gaussian profile and up-to-second-order variations in polarization degree and in position angle.

for the MP, at least in part due to the higher signal-to-noise ratio in the MP Stokes data. Consequently, we here investigate more complicated models in order to improve the goodness of the χ^2 fits to the MP Stokes data. In particular, we investigate using a multi-Gaussian function for the MP pulse profile. Table 5 lists the minimum χ^2 and degrees of freedom ν for I , Q , U , and V data sets combined and separately, followed by best-fit estimators and (1-sigma) uncertainties for the 9 polarization coefficients (p_{L0} , p'_{L0} , p''_{L0} ; ψ_0 , ψ'_0 , ψ''_0 ; p_{C0} , p'_{C0} , p''_{C0}) of the Taylor expansion through second order.

Comparison of the column “MP” in Table 3 with that in Table 4 (or, equivalently, with the column “1-Gaussian” in Table 5) finds that inclusion of the three quadratic polarization coefficients—especially p''_{L0} —reduces χ^2_Q by 42 (from 473 to 431). While $\psi''_0 = 0$ and $p''_{C0} = 0$ within statistical uncertainties, $p''_{L0} = (1.2 \pm 0.2)\%/^\circ/^\circ$ is statistically significant but small.

The main cause of the poor fit of the 1-Gaussian model to the MP data, however, has nothing to do with polarization. Figure 5 illustrates that, for the fine time resolution and

Table 2: Best-fit parameters for the MP, IP, and the LFP, using a simple Gaussian for each profile and no variations in polarization functions $p_L(\varphi)$, $\psi(\varphi)$, and $p_C(\varphi)$.

Parameter	Units	MP	IP	LFP
χ^2/ν		3400./1302	2022./1962	2518./2618
χ_I^2/ν_I		2212./324	561./489	577./653
χ_Q^2/ν_Q		477./322	534./487	674./651
χ_U^2/ν_U		441./322	463./487	603./651
χ_V^2/ν_V		269./323	463./488	664./652
I_0	$\times 1000$	1.9670 ± 0.0047	0.4414 ± 0.0044	0.0668 ± 0.0031
σ_φ	$^\circ$	1.7514 ± 0.0047	1.947 ± 0.022	3.40 ± 0.14
$\varphi_0 - \varphi_{\text{MP}}$	$^\circ$	$\equiv 0$	145.399 ± 0.023	-37.79 ± 0.14
p_{L0}	%	24.13 ± 0.19	21.24 ± 0.81	98.3 ± 5.7
$\psi_0 - \psi_{\text{MP}}$	$^\circ\text{PA}$	$\equiv 0$	1.0 ± 1.1	40.3 ± 1.2
p_{C0}	%	-1.43 ± 0.19	-2.70 ± 0.78	19.0 ± 4.0

the high signal-to-noise of the MP data, substructure in the pulse profile is quite evident. Using a 6-Gaussian (2 broad and 4 narrow) profile for $I(\varphi)$ substantially improves the fit. Comparing the column “6-Gaussian” with “1-Gaussian” in Table 5 finds that inclusion of $15 = 5 \times 3$ additional (Gaussian) parameters reduces χ_I^2 by 1415 (from 2210 to 795). Even so, the fit to the Stokes data is not formally acceptable.

It is important to note that the best-fit expectation values and uncertainties for the polarization coefficients (p_{L0} , p'_{L0} , p''_{L0} ; ψ_0 , ψ'_0 , ψ''_0 ; p_{C0} , p'_{C0} , p''_{C0}) are rather insensitive to details of the pulse profile. Thus, we compensate for fine substructure in the pulse profile by increasing the estimators for the measurement standard deviations until a statistically acceptable fit is achieved. That is, we adjust σ_I , σ_Q , σ_U , and σ_V until (Eq. A1) χ_I^2/ν_I , χ_Q^2/ν_Q , χ_U^2/ν_U , and χ_V^2/ν_V , respectively, are close to unity. The column “1-Gaussian (Adj.)” in Table 5 shows the best-fit polarization parameters for a single-Gaussian profile, with weightings adjusted as described. The only noticeable effect of this adjustment upon the best-fit polarization parameters is a small change—typically an increase—in their uncertainties. The uncertainties quoted in Table 1 (§3) are the typically more conservative values obtained using the single-Gaussian profiles and adjusted weightings.

Table 3: Best-fit parameters for the MP, the IP, and the LFP, using a simple Gaussian for each profile and up-to-linear variations in polarization functions $p_L(\varphi)$, $\psi(\varphi)$, and $p_C(\varphi)$.

Parameter	Units	MP	IP	LFP
χ^2/ν		3395./1299	2017./1959	2517./2615
χ_I^2/ν_I		2212./324	561./489	577./653
χ_Q^2/ν_Q		473./320???	532./485	674./649
χ_U^2/ν_U		440./320	462./485	602./649
χ_V^2/ν_V		269./322	463./487	664./651
I_0	$\times 1000$	1.9669 ± 0.0047	0.4415 ± 0.0044	0.0668 ± 0.0031
σ_φ	$^\circ$	1.7514 ± 0.0047	1.946 ± 0.022	3.40 ± 0.14
$\varphi_0 - \varphi_{\text{MP}}$	$^\circ$	$\equiv 0$	145.389 ± 0.023	-37.74 ± 0.20
p_{L0}	%	24.13 ± 0.19	21.25 ± 0.81	98.3 ± 5.7
p'_{L0}	%/ $^\circ$	-0.32 ± 0.16	1.09 ± 0.59	-0.9 ± 2.4
$\psi_0 - \psi_{\text{MP}}$	$^\circ\text{PA}$	$\equiv 0$	0.9 ± 1.1	40.3 ± 1.2
ψ'_0	$^\circ\text{PA}/^\circ$	-0.14 ± 0.18	0.91 ± 0.78	-0.18 ± 0.48
p_{C0}	%	-1.43 ± 0.19	-2.70 ± 0.78	19.0 ± 4.0
p'_{C0}	%/ $^\circ$	-0.01 ± 0.15	0.38 ± 0.57	0.3 ± 1.7

Table 4: Best-fit parameters for the MP, for the IP, and for the LFP, using a simple Gaussian for each profile and up-to-quadratic variations in polarization functions $p_L(\varphi)$, $\psi(\varphi)$, and $p_C(\varphi)$.

Parameter	Units	MP	IP	LFP
χ^2/ν		3348./1296	2016./1956	2517./2612
χ_I^2/ν_I		2210./324	561./489	577./653
χ_Q^2/ν_Q		431./318	531./483	674./647
χ_U^2/ν_U		440./318	461./483	603./647
χ_V^2/ν_V		268./321	462./486	664./650
I_0	$\times 1000$	1.9713 ± 0.0047	0.4414 ± 0.0045	0.0666 ± 0.0034
σ_φ	$^\circ$	1.7436 ± 0.0048	1.947 ± 0.023	3.42 ± 0.20
$\varphi_0 - \varphi_{\text{MP}}$	$^\circ$	$\equiv 0$	145.389 ± 0.023	-37.75 ± 0.20
p_{L0}	%	23.20 ± 0.24	21.24 ± 0.99	98.1 ± 7.0
p'_{L0}	$\%/^\circ$	-0.32 ± 0.16	1.03 ± 0.59	-0.9 ± 2.4
p''_{L0}	$\%/^\circ/^\circ$	1.21 ± 0.18	-0.04 ± 0.61	0.1 ± 1.4
$\psi_0 - \psi_{\text{MP}}$	$^\circ\text{PA}$	$\equiv 0$	-0.1 ± 1.3	40.8 ± 1.4
ψ'_0	$^\circ\text{PA}/^\circ$	-0.16 ± 0.17	0.82 ± 0.79	-0.16 ± 0.48
ψ''_0	$^\circ\text{PA}/^\circ/^\circ$	-0.06 ± 0.18	1.07 ± 0.80	-0.21 ± 0.28
p_{C0}	%	-1.26 ± 0.23	-3.15 ± 0.96	20.5 ± 4.9
p'_{C0}	$\%/^\circ$	0.01 ± 0.15	0.38 ± 0.57	0.3 ± 1.7
p''_{C0}	$\%/^\circ/^\circ$	-0.22 ± 0.17	0.47 ± 0.59	-0.49 ± 0.96

Table 5: Comparison of results of fitting the main pulse (MP) profile with a simple Gaussian, with a multi-Gaussian, and with a simple Gaussian after adjusting weightings. The models retain up-to-quadratic variations in the polarization functions $p_L(\varphi)$, $\psi(\varphi)$, and $p_C(\varphi)$.

Parameter	Units	1-Gaussian	6-Gaussian	1-Gaussian (Adj.)
χ^2/ν		3348./1296	1936./1281	1281./1296
χ_I^2/ν_I		2210./324	795./309	324./324
χ_Q^2/ν_Q		431./318	436./303	318./318
χ_U^2/ν_U		440./318	438./303	318./318
χ_V^2/ν_V		268./321	267./306	321./321
p_{L0}	%	23.20 ± 0.24	23.15 ± 0.25	23.17 ± 0.31
p'_{L0}	%/°	-0.32 ± 0.16	-0.29 ± 0.16	-0.32 ± 0.20
p''_{L0}	%/°/°	1.21 ± 0.18	1.18 ± 0.20	1.25 ± 0.24
ψ_0	°PA	-89.34 ± 0.27	-89.38 ± 0.29	-89.34 ± 0.32
ψ'_0	°PA/°	-0.16 ± 0.17	-0.19 ± 0.17	-0.16 ± 0.20
ψ''_0	°PA/°/°	-0.06 ± 0.18	0.06 ± 0.21	-0.06 ± 0.21
p_{C0}	%	-1.26 ± 0.23	-1.28 ± 0.24	-1.25 ± 0.21
p'_{C0}	%/°	-0.01 ± 0.17	-0.04 ± 0.17	-0.01 ± 0.15
p''_{C0}	%/°/°	-0.22 ± 0.17	-0.20 ± 0.19	-0.23 ± 0.16

REFERENCES

- Abdo, A. A., Ajello, M., Allafort, A., et al. 2013, *ApJS*, 208, 17
- Abdo, A. A., Allen, B. T., Atkins, R., et al. 2012, *ApJ*, 750, 63
- Aharonian, F., Akhperjanian, A. G., Bazer-Bachi, A. R., et al. 2006, *A&A*, 457, 899
- Aharonian, F., Akhperjanian, A., Beilicke, M., et al. 2004, *ApJ*, 614, 897
- Aleksić, J., Alvarez, E. A., Antonelli, L. A., et al. 2012, *A&A*, 540, A69
- Aliu, E., Arlen, T., Aune, T., et al. 2011, *Science*, 334, 69
- Allen, B. T., & Yodh, G. B. 2007, *AIP Conf. Ser.* 921, 528
- Bhat, N. D. R., Tingay, S. J., & Knight, H. S. 2008, *ApJ*, 676, 1200
- Bridle, A. H. 1970, *Nature*, 225, 1035
- Bühler, R., & Blandford, R. 2013, *arXiv:1309.7046*
- Contopoulos, I., & Kalapotharakos, C. 2010, *MNRAS*, 404, 767
- Dean, A. J., Clark, D. J., Stephen, J. B., et al. 2008, *Science*, 321, 1183
- Deutsch, A. J. 1955, *Annales d’Astrophysique*, 18, 1
- Dyks, J., Harding, A. K., & Rudak, B. 2004, *ApJ*, 606, 1125
- Dyks, J., & Rudak, B. 2003, *ApJ*, 598, 1201
- Espinoza, C. M., Guillemot, L., Çelik, Ö., et al. 2013, *MNRAS*, 430, 571
- Forot, M., Laurent, P., Grenier, I. A., Gouiffès, C., & Lebrun, F. 2008, *ApJ*, 688, L29
- Gould, D. M., & Lyne, A. G. 1998, *MNRAS*, 301, 235
- Hankins, T. H., Kern, J. S., Weatherall, J. C., & Eilek, J. A. 2003, *Nature*, 422, 141
- Jones, D. H. P., Smith, F. G., & Wallace, P. T. 1981, *MNRAS*, 196, 943
- Kalapotharakos, C., Kazanas, D., Harding, A., & Contopoulos, I. 2012, *ApJ*, 749, 2
- Karastergiou, A., & Johnston, S. 2006, *MNRAS*, 365, 353
- Karuppusamy, R., Stappers, B., & van Straten, W. 2008, *PASP*, 120, 191

- Karuppusamy, R., Stappers, B. W., & van Straten, W. 2010, *A&A*, 515, A36
- Kuiper, L., Hermsen, W., Cusumano, G., et al. 2001, *A&A*, 378, 918
- Li, J., Spitkovsky, A., & Tchekhovskoy, A. 2012, *ApJ*, 746, 60
- Lyne, A. G., & Graham-Smith, F. 2006, *Pulsar Astronomy*, 3rd ed. (Cambridge, UK: Cambridge University Press), ISBN 0521839548
- Lyne, A., Graham-Smith, F., Weltevrede, P., et al. 2013, *Science*, 342, 598
- Majid, W. A., Naudet, C. J., Lowe, S. T., & Kuiper, T. B. H. 2011, *ApJ*, 741, 53
- Manchester, R. N. 1971, *ApJS*, 23, 283
- Manchester, R. N., Hobbs, G. B., Teoh, A., & Hobbs, M. 2005, *AJ*, 129, 1993
- Moffett, D. A., & Hankins, T. H. 1996, *ApJ*, 468, 779
- Moffett, D. A., & Hankins, T. H. 1999, *ApJ*, 522, 1046
- Moran, P., Shearer, A., Gouiffès, C., & Laurent, P. 2014, arXiv:1302.3622 (2013)
- Moran, P., Shearer, A., Mignani, R. P., et al. 2013, *MNRAS*, 433, 2564
- Muslimov, A. G., & Harding, A. K. 2004, *ApJ*, 606, 1143
- Oort, J. H., & Walraven, T. 1956, *Bull. Astron. Inst. Netherlands*, 12, 285
- Pétri, J., & Kirk, J. G. 2005, *ApJ*, 627, L37
- Pierbattista, M., et al. 2013, in preparation
- Radhakrishnan, V., & Cooke, D. J. 1969, *Astrophys. Lett.*, 3, 225
- Romani, R. W., & Watters, K. P. 2010, *ApJ*, 714, 810
- Romani, R. W., & Yadigaroglu, I.-A. 1995, *ApJ*, 438, 314
- Silver, E. H., Kestenbaum, H. L., Long, K. S., et al. 1978, *ApJ*, 225, 221
- Słowikowska, A., Kanbach, G., Kramer, M., & Stefanescu, A. 2009, *MNRAS*, 397, 103
- Smith, F. G., Jones, D. H. P., Dick, J. S. B., & Pike, C. D. 1988, *MNRAS*, 233, 305
- van Straten, W., & Bailes, M. 2011, *PASA*, 28, 1

- van Straten, W., Demorest, P., & Osłowski, S. 2012, *Astron. Research & Technology*, 9, 237
- Venter, C., Johnson, T. J., & Harding, A. K. 2012, *ApJ*, 744, 34
- Weltevrede, P., & Johnston, S. 2008, *MNRAS*, 391, 1210
- Wolfram Research, Inc. 2013, *Mathematica*, Version 9.0 (Champaign, IL: Wolfram Research)
- Woltjer, L. 1957, *Bull. Astron. Inst. Netherlands*, 13, 301